




# Electrocatalytic layers for hydrogen evolution reaction based on nickel phosphides: cost-effective fabrication and XPS characterization

Roberto Bernasconi<sup>1,\*</sup> , Mohammed Ibrahim Khalil<sup>1</sup>, Dogukan Selahattin Cakmakci<sup>1</sup>, Yagmur Bektas<sup>1</sup>, Luca Nobili<sup>1</sup>, Luca Magagnin<sup>1</sup>, and Cristina Lenardi<sup>2</sup>

<sup>1</sup>Dipartimento di Chimica, Materiali e Ing. Chimica "Giulio Natta", Politecnico Di Milano, Via Mancinelli 7, 20131 Milan, Italy

<sup>2</sup>C.I.Ma.I.Na., Dipartimento di Fisica "Aldo Pontremoli", Università Di Milano, Via Celoria 16, 20133 Milan, Italy

Received: 7 January 2022

Accepted: 19 April 2022

Published online:

16 May 2022

© The Author(s) 2022

## ABSTRACT

The development of efficient electrocatalysts based on Pt-free materials is a crucial step for the maturation of competitive water splitting technologies able to sustain the upcoming hydrogen-based economy. In this context, the present work optimizes a codeposition/annealing methodology to produce electrocatalytic layers for the hydrogen evolution reaction (HER) based on one of the most promising alternatives to Pt-based catalysts: nickel phosphides. A nickel-phosphorus solid solution is codeposited with red phosphorus microparticles and the obtained composites are annealed to promote interdiffusion and reaction between nickel and phosphorus. The experimentation carried out demonstrates that the properties of the final phosphide layers depend on the conditions employed in both the codeposition step and the annealing step. It is fundamental to evaluate and optimize the NiP/P codeposition process, and it is also important to understand the influence of annealing time and temperature on the microstructure and HER performance of the layers obtained. X-ray photoelectron spectroscopy (XPS) is employed to evaluate the phase composition at the surface, highlighting the presence of a top layer characterized by a Ni<sub>2</sub>P/Ni<sub>12</sub>P<sub>5</sub> ratio significantly lower than the value found in the bulk of the coating. Annealed NiP/P layers are tested for HER in 0.5 M sulphuric acid solution. The tests demonstrate a clear correlation between the Ni<sub>2</sub>P/Ni<sub>12</sub>P<sub>5</sub> ratio on the surface and the overpotential for HER. Coherently, when the outer Ni<sub>12</sub>P<sub>5</sub>-rich layer is mechanically removed, lower overpotentials are observed (169.5 mV vs. RHE for 10 mA cm<sup>-2</sup>).

Handling Editor: Joshua Tong.

Address correspondence to E-mail: roberto.bernasconi@polimi.it

## Introduction

Renewable energy sources are strategic for the green revolution currently underway. Their use in place of fossil fuels allows to minimize environmental impact, generating few greenhouse emissions and sustaining the future economic and social needs [1]. Consequently, renewable technologies are currently gaining increasing importance over the years. Their exploitation involves two important steps: production and storage. The latter is fundamental especially in the case of sources characterized by an intrinsic intermittency, like solar or wind. Storage technologies can be chemical, electrochemical, mechanical, electrical, or thermal [2]. Given their strategic value, research and development on electrochemical techniques for clean energy storage dramatically gained importance [3] and nowadays electrochemically generated hydrogen stands out as one of the most promising energy storage mediums [4]. Indeed, hydrogen has a fundamental role in energy conversion based on fuel cells [5]. Moreover, hydrogen presents attractive advantages as an energy storage medium: it does not involve dangerous emissions, it can be easily produced from water [6] and it is characterized by high specific energy (33.3 kWh kg<sup>-1</sup> for liquid hydrogen) [7]. On Earth, most of the hydrogen exists in molecular forms like water or organic compounds. However, hydrogen can be produced exploiting water electrolysis (WE) [8], where water splits into H<sub>2</sub> and O<sub>2</sub>. The hydrogen evolution reaction (HER; 2 H<sub>2</sub>O + 2 e<sup>-</sup> → H<sub>2</sub> + 2 OH<sup>-</sup>) takes place at the cathode, while the oxygen evolution reaction (OER; 4 OH<sup>-</sup> → O<sub>2</sub> + 2 H<sub>2</sub>O + 4 e<sup>-</sup>) takes place at the anode.

In normal conditions, a considerable electrochemical overpotential is needed to trigger HER on the electrode surface [9]. Therefore, highly efficient WE requires the use of an electrocatalyst to minimize the energy barrier associated with HER, and hence the overpotential. Generally, noble metals like Pt or Pd are regarded as the best electrocatalysts for HER due to their excellent activity in acidic environment [10]. On the other hand, their high cost and insufficient availability induced researchers to explore possible cost-effective alternatives. Therefore, research focused on the quest for materials alternative to Pt [11], which is the most popular catalyst due to its high electrocatalytic activity and robust stability

[12, 13]. Nowadays, alternative low-cost electrocatalytic materials are continuously discovered and some of them have been significantly developed. Crucial examples are some transition metals or alloys [14, 15] and their nanoparticles (NP) [16, 17], metal sulphides [18], selenides [19], phosphides [20–25], nitrides [26] and carbides [26].

In the present work, nickel phosphide is considered as an electrocatalytic material and examined in the form of thin film. Nickel phosphide is one of the most promising electrocatalytic materials and can be evaluated as a replacement of Pt-based catalysts in the future. Research demonstrates that all the existing compounds of Ni and P have some catalytic activity [20, 27, 28]. This mainly depends on the P content [29, 30] and the form of the catalyst. According to the literature, nickel phosphides showed good stability and low HER overpotentials, especially in the case of the Ni<sub>2</sub>P compound [20, 31]. For instance, Read et al. [32] indicated an overpotential of 128 mV at 10 mA/cm<sup>2</sup> for Ni<sub>2</sub>P, which was obtained through the reaction of commercially available Ni metal foils with various organophosphine reagents. Besides phosphine-based chemical synthesis, which is highly noxious, alternative methods to produce Ni<sub>2</sub>P have been identified. Specifically, nickel phosphide has been produced, in the form of NPs or nanowires, via the decomposition of metal–phosphine moieties [31], by solvothermal [33, 34] or hydrothermal synthesis [35, 36] and by direct phosphorization of Ni [37–39]. Other nickel–phosphorus compounds, like Ni<sub>3</sub>P or Ni<sub>12</sub>P<sub>5</sub>, are characterized by interesting electrocatalytic properties [20]. However, Ni<sub>2</sub>P exhibits better HER performance due to the higher phosphorous content [29].

Nickel phosphide thin films can be obtained by direct phosphorization of Ni prepared via electrodeposition or sputtering [40, 41]. However, this production process generally involves the presence of poisonous precursors, like gaseous elemental phosphorus at high temperature or phosphine [42]. These species are highly dangerous since they can potentially cause the formation of the white P allotrope, which is highly toxic and explosive [43]. In addition to this, P usage is generally not optimized with these processes, resulting in excessive material waste. In this context, we recently developed an innovative manufacturing strategy for electrocatalytic Ni<sub>2</sub>P thin films [44]. We employed electrodeposition to codeposit a metastable NiP solid solution matrix with

elemental red P microparticles, thus overcoming the compositional limit on P content typical of electrolytic deposition [45, 46]. Then, we annealed the resulting composites to promote P interdiffusion and compound formation. This method is safe because formation of white P is prevented by incorporating all the elemental P inside the coating and making it react during the annealing treatment, with negligible P leakage into the atmosphere. Optimal P usage can be guaranteed with this method. Annealing parameters were optimized to minimize oxidation, to provide the best conditions for Ni<sub>2</sub>P formation and to minimize the growth of secondary phases. As a result, an overpotential of 224 mV at 10 mA/cm<sup>2</sup> was obtained.

In the present work, we improved the fabrication methodology previously developed by optimizing the codeposition step and gaining deeper insight into the structure of the layers produced. To accomplish the first goal, the granulometry of the red P particles was controlled to favour their dispersion in the electrolyte and their codeposition in the coating. Secondly, we provided a deeper understanding of the phosphide formation mechanisms that take place during annealing by performing X-ray photoelectron spectroscopy (XPS) analysis. XPS can provide information about elements distribution and chemical state up to around 10 nm below the surface [47]. This is the ideal condition for studying the surface of the electrocatalyst, which is the part that interacts with the electrolyte during HER. XPS has been widely employed in the literature to determine the presence of oxides on the surface and to identify the chemical state of the elements present in the catalytic material [48–50]. Furthermore, Xin et al. demonstrated that different nickel–phosphorus compounds can be identified by mean of XPS, allowing to precisely determine the phase composition of the first nm of material close to the surface [51]. By performing XPS measurements, the effect of annealing time and temperature, as well as initial P content on the properties of the electrocatalysts was investigated. As a result of the better understanding of the mechanism leading to Ni<sub>2</sub>P formation, we were able to push the HER performances of the layers to levels comparable to those of pure Ni<sub>2</sub>P.

## Experimental methods

### Red P particles sedimentation process

All the chemicals employed were acquired from Sigma-Aldrich and used as received. For the filtration process, 200 mL of distilled water was poured in a beaker. Later, 40 g of red phosphorus was added, stirred for five minutes and then placed for 10 min in an ultrasonic bath. After this process, the dispersed solution was poured into a 250 mL cylinder. After 45 s, the solution was poured into another glass from the sedimentation cylinder, leaving thus big sized particles at the bottom of the cylinder. The resulting solution was filtered using filter paper. When filtration was complete, particles were removed from the filter paper and dried on a heater at about 60 °C.

### NiP/P layer electrodeposition process

The electrolyte employed for NiP/P electrodeposition was a modified Watts bath in which the red P particles previously prepared were dispersed. The modified Watts bath was formulated as follows: 180 g L<sup>-1</sup> of NiSO<sub>4</sub>·6H<sub>2</sub>O, 24 g L<sup>-1</sup> of NiCl<sub>2</sub>·6H<sub>2</sub>O, 30 g L<sup>-1</sup> of H<sub>3</sub>PO<sub>4</sub> and 20 g L<sup>-1</sup> of H<sub>3</sub>PO<sub>3</sub>. pH of the electrolyte was corrected to 2 using NaOH. Before performing electrodeposition, settled red P particles were added to the bath in the following amounts: 10 g L<sup>-1</sup>, 20 g L<sup>-1</sup>, 40 g L<sup>-1</sup>, 50 g L<sup>-1</sup> and 100 g L<sup>-1</sup>. NiP/P deposition was performed for 2 h at 20 mA cm<sup>-2</sup>, 50 °C and vigorous stirring. Copper plates were employed as substrate and pure nickel was the anode. Before deposition, copper was cleaned with acetone and deoxidized with a 6.5% HNO<sub>3</sub> solution (immersion time of 5 s). At the end of the deposition step, the samples were washed with demineralized water to eliminate residual P particles and dried with N<sub>2</sub>.

### Annealing process

Annealing was performed in a Carbolite tubular furnace, with a N<sub>2</sub> protective atmosphere. Annealing time was varied between 1 and 4 h and temperature was varied between 300 and 400 °C, as detailed afterwards.

## Layers characterization

Scanning electron microscopy (SEM) was performed using a Zeiss EVO 50 electron microscope, equipped with an Oxford Instruments 7060 EDS module.

To prepare the cross sections, samples were cut, incorporated in the epoxy resin and polished to a mirror-like finish. Transmission electron microscopy (TEM) analysis was performed employing a Philips CM 200 instrument. X-ray diffraction (XRD) spectra were acquired using a Philips PW 1830 diffractometer in glancing angle configuration with Cu  $K_\alpha$  radiation ( $\lambda = 1.5406 \text{ \AA}$ ).

## XPS characterization

XPS measurements were carried out with a PHI 5600 UHV apparatus equipped with a monochromatized X-ray source (Al  $K_\alpha = 1486.6 \text{ eV}$ ,  $\Delta E = 0.48 \text{ eV}$ ). Pressure in the chamber was less than  $1.2 \times 10^{-9}$  mbar during data acquisition. High-resolution spectra were acquired in constant step energy mode ( $E_{\text{pass}} = 23.8 \text{ eV}$ ). The overall energy resolution was 0.8 eV. The binding energy scale was calibrated using the Au  $4f_{7/2}$  core level line (83.96 eV) of a clean polycrystalline Au sample. When specified, the samples were sputtered at selected time intervals with a PHI 04-303 differential ion gun. Argon was employed and the ion energy was set at 2 keV with ion current on the sample in the order of  $5 \mu\text{A}$  (pressure in the chamber around  $1 \times 10^{-8}$  mbar). Least square fitting was performed using the programs KolXPD and Igor Pro. A standard Shirley background was used to fit the background, while the peaks were fitted using Voigt curves.

## Electrochemical characterization

Electrocatalysis tests were carried out using the annealed NiP/P layers as working electrode in an electrochemical cell containing graphite as counter electrode and a 3 M KCl Ag/AgCl standard reference electrode. A 0.5 M  $\text{H}_2\text{SO}_4$  solution was used as electrolyte during the tests. All the measurements were performed at ambient temperature and under vigorous stirring. The potential was varied at a constant rate of 2 mV/s in all the tests. No Ohmic correction was applied, but the reference electrode was kept close to the working electrode to limit voltage drops. A standard 20 wt% Pt catalyst was characterized

together with the samples produced and was used as a reference material to compare electrocatalytic properties.

## Results and discussion

### NiP/P codeposition optimization

As described in a previous paper [44], the first part of the electrocatalyst manufacturing process is the codeposition of a NiP matrix (a solid solution of the two elements) with particles of elemental red P. The second step is a controlled annealing treatment able to promote interdiffusion and phosphide formation. It was observed that the exposure to high temperatures, which are essential for achieving acceptable diffusion rates, considerably decreased P concentration in the electrodeposited layers. This effect, which is essentially driven by premature P evaporation, can be counterbalanced by maximizing the amount of red P codeposited with the NiP matrix.

To this extent, the first step required to optimize the P content is a precise determination of the codeposition rate as a function of the amount of P in the bath. In the previous paper, we simply dispersed  $200 \text{ g L}^{-1}$  of red P in the NiP bath, subsequently performing sedimentation to remove larger particles directly in the electrolyte. In this way, however, the final concentration of P particles in the bath was unknown and hardly controllable. Indicatively, the P concentration decreased to roughly  $70 \text{ g L}^{-1}$  at the end of the sedimentation process. A possible approach to improve process reproducibility was P sedimentation in water. Red P particles were dispersed in water and then subjected to the sedimentation process. The resulting dispersion was then filtered and the red P particles were dried in air. By doing this, it was possible to weight precise amounts of particles and add them to the NiP electrolyte.

Figure 1a depicts the effect of P concentration in the electrolyte on P concentration in the deposited layer. Obviously, the graph does not start from the origin because the material deposited at  $0 \text{ g L}^{-1}$  of red P always contains some P in the form of solid solution with Ni. The graph also shows the effect of the addition of unsettled, one time settled, or two times settled P particles. As expected from an electrolytic codeposition process, the relative P concentration in the layer increased as P concentration in the



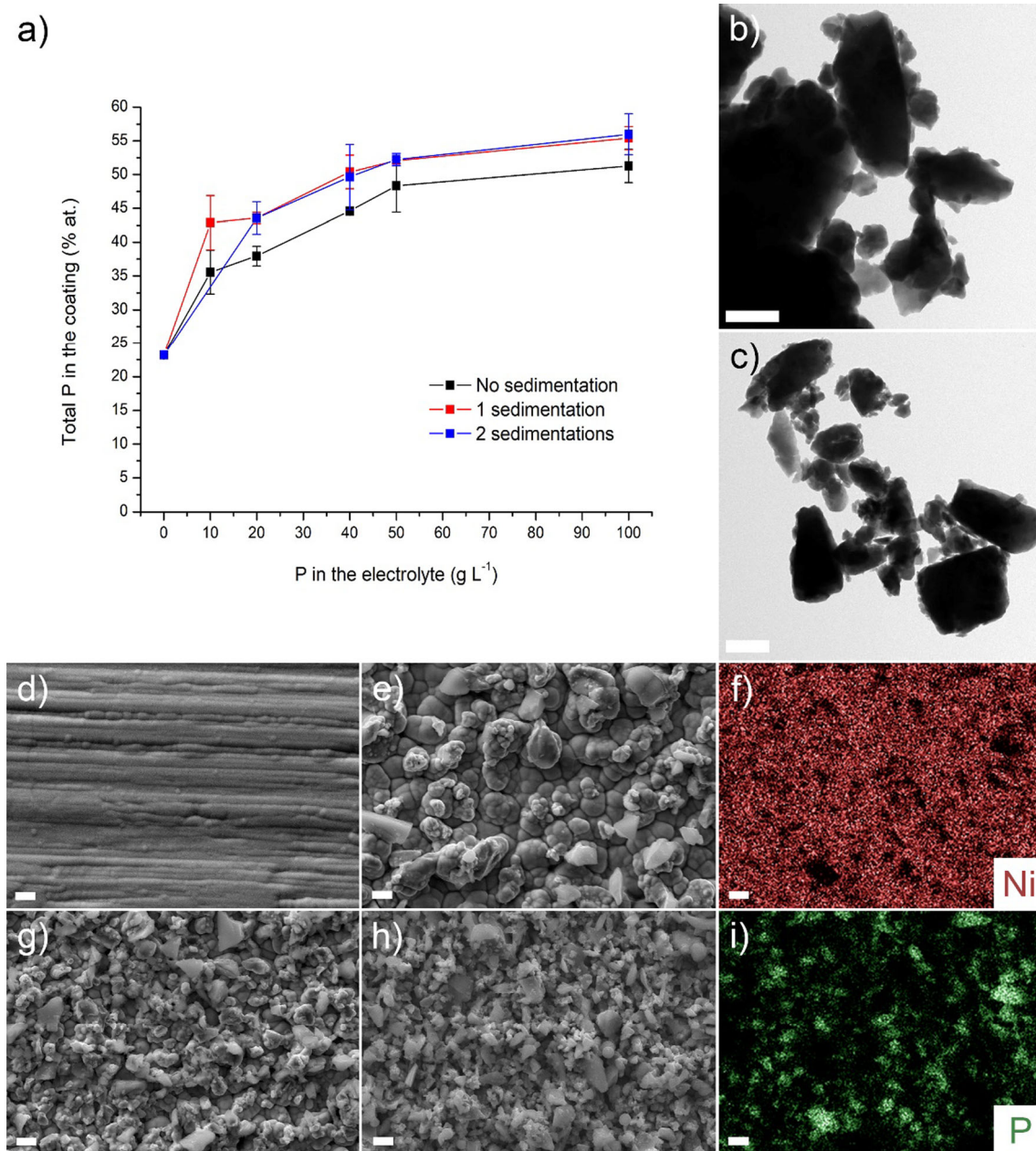


**Figure 1** Codeposition graph for red P in the Ni/P composite (a); TEM image of unsettled red P microparticles (b), TEM image of double settled red P microparticles (c), SEM images of Ni/P layers plated from a bath containing 0 g L<sup>-1</sup> (d), 10 g L<sup>-1</sup> (e),

40 g L<sup>-1</sup> (g) and 100 g L<sup>-1</sup> (h) double settled red P; EDS elemental mapping for Ni (f) and P (i) of a sample plated from a bath containing 100 g L<sup>-1</sup> of red P. Scale bars are as follow: 500 nm (b, c), 4 μm (d–i).

bath increased and reached a plateau. This behaviour has been rationalized in a great number of mathematical models [52, 53], the most famous one being Guglielmi's model [54, 55]. Guglielmi assumed that the amount of codeposited particles depends on the competition between two phenomena taking place on the surface of the growing composite: electrophoresis

and adsorption. Starting from this premise, he developed Eq. 1 [55].

$$\frac{C}{\alpha} = \frac{MJ_0}{nFdV_0} e^{\eta(A-B)} \left( \frac{1}{k} + C \right) \quad (1)$$

$\alpha$  is the volumetric percentage of particles in the deposit,  $C$  is the volumetric percentage of particles in the bath,  $\eta$  is the overpotential,  $F$  is the Faraday

constant,  $J_0$  is the exchange current density,  $k$  is the coefficient of adsorption,  $d$ ,  $M$  and  $n$  are density, molar mass and valence of the metal/alloy deposited, respectively.  $A$ ,  $B$  and  $V_0$  are constants. Higher particle concentrations favour the adsorption contribution, resulting into higher codeposition rates (as evident from Eq. 1). The second effect observed during the tests was an improvement of codeposited P percentage in the case of settled particles. The rationalization of this effect requires the determination of the size distribution of the particles before and after the sedimentation process. Consequently, different TEM images were acquired for unsettled, singly settled and double settled red P particles. From the qualitative point of view, unsettled P particles were characterized by a broad range of diameters (Fig. 1b). The presence of many large particles, over 2–2.5  $\mu\text{m}$ , was observed. On the contrary, in the case of single and double settlement, such large particles were almost absent (Fig. 1c). Size distribution graphs were built by analysing an adequate number of TEM images (figures S1, S2 and S3). These graphs quantitatively demonstrate that the sedimentation process removed larger particles and significantly reduced the size dispersion of the microparticles. No real differences were observed in the size distribution after one or two sedimentation steps, and this explains the behaviour visible in Fig. 1a, that is the amounts of codeposited P for singly settled and double settled particles are comparable. From these results, it is evident that singly and double settled particles on average are smaller than their unsettled counterparts. According to the codeposition process considered, smaller particles can codeposit better, resulting in higher codeposition rates. This behaviour has been observed, for example, in the case of codeposition of diamond particles with Ni [56]. By fitting the experimental data for settled solutions in Fig. 1a with the model described by Eq. 1, the presence of a plateau is evident (figure S4). Any further increase of P concentration in the bath would result in a negligible increase of the concentration in the layer.

The effect of increasing amounts of P in the electrolyte on the quantity of codeposited P is also evident in SEM observation of the layer surface. Figure 1d, e, g, h show the appearance of NiP/P layers deposited from solutions containing 0  $\text{g L}^{-1}$ , 10  $\text{g L}^{-1}$ , 40  $\text{g L}^{-1}$  and 100  $\text{g L}^{-1}$  of P particles, respectively.

The surface of the composite became increasingly rough with increasing amounts of codeposited P particles. Their presence can be clearly seen by looking at Fig. 1f, i, which depict the EDS elemental maps of Ni and P, respectively. Even though phosphorous is scattered uniformly on the surface due to its presence in the solid solution matrix, most of the element is concentrated in micrometric areas that correspond to the red P particles.

Theoretically, red P content in the deposit can be increased also by varying the current density (Eq. 1). However, in the case of NiP deposition, too high current densities negatively affect the cathodic efficiency of the deposition process, which is already relatively low (54%) due to the high P content of the solid solution [57]. Consequently, current density was kept constant and only red P concentration in the bath was varied. The resulting optimized red P concentration in the deposit, 56.0 at%, was reached at 100  $\text{g L}^{-1}$  of singly settled red P in the bath.

### Annealing optimization

After codeposition, NiP/P layers were annealed in a  $\text{N}_2$  atmosphere. According to our previous results, the final phase composition strongly depended on the parameters used for the annealing treatment. Indeed, the nickel–phosphorus phase diagram [58] describes the possible formation of many compounds ( $\text{Ni}_3\text{P}$ ,  $\text{Ni}_{12}\text{P}_5$ ,  $\text{Ni}_2\text{P}$ ,  $\text{Ni}_5\text{P}_4$ ,  $\text{NiP}$ ,  $\text{NiP}_2$ ). Due to the complexity of such phase diagram and to the observed tendency of the layer to lose increasing amounts of P at increasing temperatures, a correlation between annealing conditions and final phase composition can be easily rationalized. At high temperatures, the layer is strongly depleted of elemental P, which evaporates before reacting to form compounds. Consequently, only compounds containing a low atomic percentage of P can form. In our previous paper, the temperature of 300  $^\circ\text{C}$  was identified as a good compromise for reducing P evaporation without decreasing too much solid-state diffusivity. However, in the present work initial P content was higher because of the optimized codeposition procedure adopted.

Morphology and elemental composition of the layers were evaluated by SEM observation and EDS analysis after performing different annealing treatments. Regardless of initial P concentration and annealing conditions, the layers exhibited a similar

morphology, as shown in Fig. 2a, b. These images depict the post-annealing morphology of samples plated from the same bath ( $100 \text{ g L}^{-1}$  of red P) and annealed at  $400 \text{ }^\circ\text{C}$  for 1 h (Fig. 2a) or at  $300 \text{ }^\circ\text{C}$  for 2 h (Fig. 2b). In both cases, the surface morphology is characterized by high roughness and a certain degree of porosity, reasonably left by evaporated P particles. EDS elemental mapping revealed a uniform

distribution of Ni and P on the surface of the layer. To characterize the zones of the coating far from the surface, samples were mounted in epoxy resin and sectioned. Figure 2c shows the cross section of the sample annealed at  $300 \text{ }^\circ\text{C}$  for 2 h. A uniform distribution of the elements along the thickness is evidenced (figure S5) and no sign of residual P in the coating is found. If compared to our previous paper

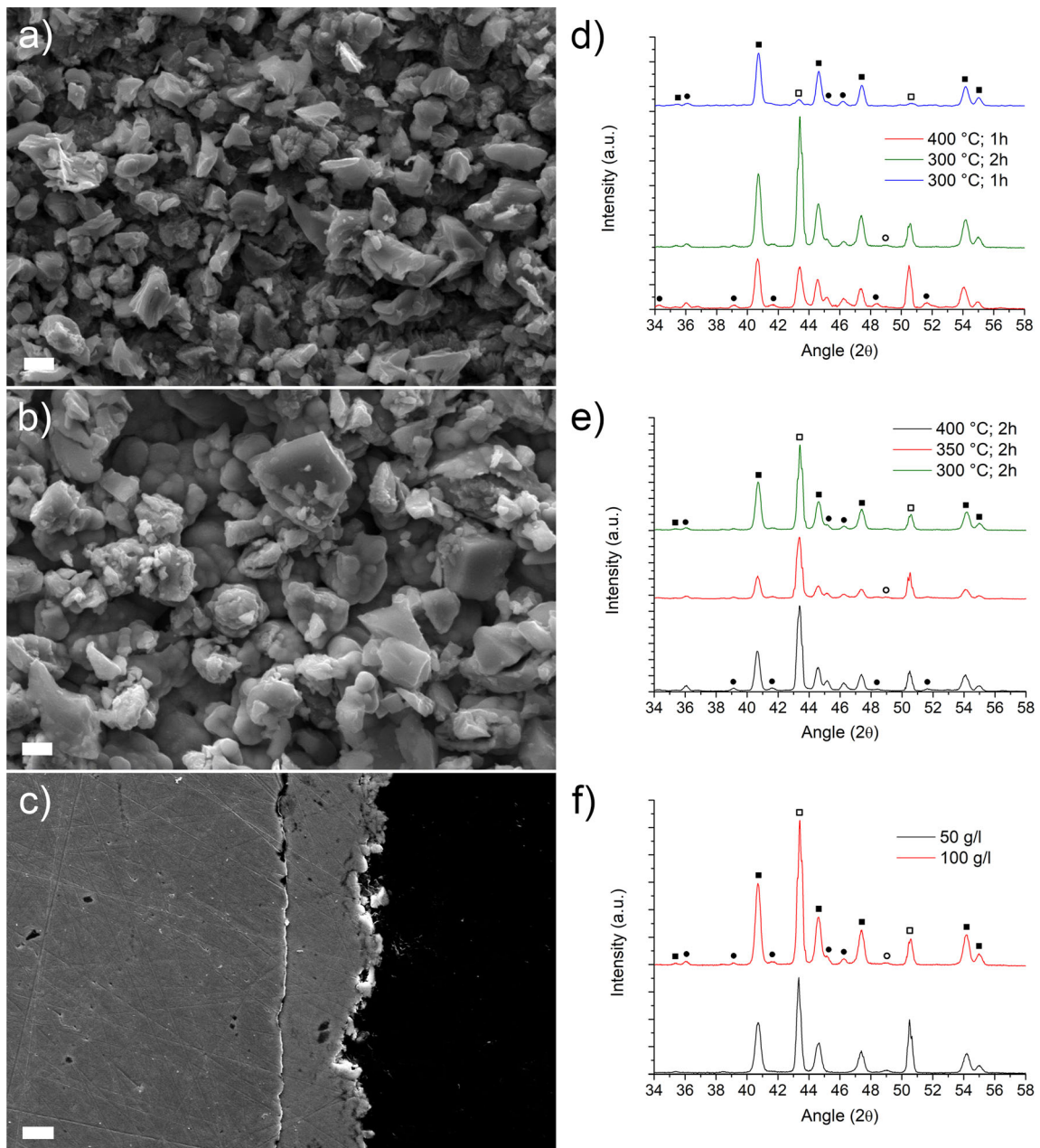


**Figure 2** SEM image of a sample plated from a  $100 \text{ g L}^{-1}$  P bath and annealed at  $400 \text{ }^\circ\text{C}$  for 1 h (a); SEM top view (b) and cross section (c) of a sample plated from a  $100 \text{ g L}^{-1}$  P bath and annealed at  $300 \text{ }^\circ\text{C}$  for 2 h; XRD characterization of NiP/P layers

annealed under different conditions (d–f). Phases are identified by the following symbols: empty squares for the Cu substrate, filled squares for  $\text{Ni}_2\text{P}$ , empty circles for  $\text{Ni}_{12}\text{P}_5$  and filled circles for  $\text{Cu}_3\text{P}$ . Scale bars are as follow:  $2 \mu\text{m}$  (a, b),  $4 \mu\text{m}$  (c).



[44], the layers obtained were characterized by some residual porosity (Fig. 2c and Figure S6). This is reasonably a consequence of the higher P content achieved in the present work, which probably resulted in some minor porosity when P interdiffused and evaporated during the annealing step.

From the compositional point of view, EDS characterization of the samples before and after annealing produced the data reported in Table 1. Final P concentration depended on annealing time and temperature, with values ranging between 53.2 at.% for the sample annealed at 300 °C for 1 h and 34.4 at.% for the sample annealed at 400 °C for 2 h.

### XRD characterization

Obviously, as expected by considering the Ni–P phase diagram [58], different levels of P in the coating translate into different phases. Consequently, phase composition of the layers was determined using XRD. The non-annealed NiP/P composite was found to be amorphous, as evident from figure S7, where only Cu peaks from the substrate are visible. This is a consequence of the amorphous nature of red P and the high concentration of P in the solid solution (figure S9). Nickel phosphides formed during the annealing process carried out on the sample after the deposition step. In general, peak identification demonstrated the existence of the two phases Ni<sub>2</sub>P and Ni<sub>12</sub>P<sub>5</sub>, which were expected to form by comparing the P amount present in the samples with the phase stability ranges reported in the Ni–P phase diagram. Diffraction peaks of Ni<sub>2</sub>P (JCPDS ref. code 00-013-0213) are located at 40.8° (111), 44.6° (201), 47.3° (210), 54.2° (300), 54.9° (211), 66.2° (310), 72.7° (311), 74.7° (400) and 80.9° (401). The most intense

peaks of Ni<sub>12</sub>P<sub>5</sub> (JCPDS ref. code 00-022-1190) are: 20.5° (200), 29.0° (211), 32.7° (310), 38.4° (112), 41.6° (321), 41.7° (400), 44.4° (330), 47.0° (420), 49.0° (312), 56.2° (501), 60.1° (422) and 68.6° (620).

In general, the dominant phase in all the samples is Ni<sub>2</sub>P. This is not unexpected, since all the samples exhibit P contents larger than the value typical of this Ni–P compound (33.33 at.%). However, depending on the specific annealing conditions, the presence of minor amounts of secondary phases was recorded. Figure 2d describes the effect of different annealing times on the phase composition of the layers plated from the 100 g L<sup>-1</sup> P electrolyte. The intensity of the Ni<sub>12</sub>P<sub>5</sub> peaks increased with the annealing time. The sample annealed at 300 °C for 1 h presented an almost negligible Ni<sub>12</sub>P<sub>5</sub> amount, whereas the sample annealed for 2 h exhibited a minor amount of this phase. The same considerations are valid for the sample annealed at 400 °C for 1 and 2 h. Unlike our previous paper, the samples hereby analysed were characterized by the presence of a secondary phase, Cu<sub>3</sub>P (JCPDS ref. code 71-2261). The formation of this phase is realistically connected to the high amount of P present in the layer, which reacts with Cu at the interface between the substrate and the coating and forms copper phosphide. At low annealing times and temperatures (300 °C; 1 h), the kinetics of Cu<sub>3</sub>P formation are presumably sluggish and the sample did not contain any detectable trace of this phase. Figure 2e describes the effect of increasing annealing temperatures on the phase composition of the samples annealed for 2 h. An increase in the relative contribution of Cu<sub>3</sub>P with temperature can be seen in the diffraction patterns. Some residual Ni<sub>12</sub>P<sub>5</sub> can be detected in all the samples. Obviously, increasing

**Table 1** Composition and mean crystallite size of NiP/P layers before and after annealing

| P concentration in the bath (g L <sup>-1</sup> ) | Annealing temperature (°C) | Annealing time (h) | Concentration of P in the layer before annealing (at.%) | Concentration of P in the layer after annealing (at.%) | Mean crystallite size (nm) |
|--|----------------------------|--------------------|---|--|----------------------------|
| 50   | 300                        | 2                  | 52.2  | 42.8   | 32.6                       |
| 50   | 300                        | 4                  | 52.2  | 41.1   | 34.9                       |
| 100  | 300                        | 1                  | 56.0  | 53.2   | 35.4                       |
| 100  | 300                        | 2                  | 56.0  | 51.7   | 36.1                       |
| 100  | 350                        | 2                  | 56.0  | 40.5   | 37.0                       |
| 100  | 400                        | 2                  | 56.0  | 34.4   | 40.2                       |
| 100  | 400                        | 1                  | 56.0  | 38.6   | 37.7                       |



temperatures considerably favoured the formation of  $\text{Cu}_3\text{P}$ , which is more present in the sample annealed at 400 °C. Figure 2f depicts the effect of two different initial P concentrations on the layer composition after annealing at 300 °C for 2 h. The initial concentrations were 52.2 and 56.0 at.%, obtained from the baths containing 50 g L<sup>-1</sup> and 100 g L<sup>-1</sup>, respectively. The sample plated from the 50 g L<sup>-1</sup> bath contained a significant amount of  $\text{Ni}_{12}\text{P}_5$  and no detectable traces of  $\text{Cu}_3\text{P}$ . Conversely, the sample plated from the 100 g L<sup>-1</sup> bath was characterized by less intense peaks of  $\text{Ni}_{12}\text{P}_5$ , together with the presence of  $\text{Cu}_3\text{P}$ . Evidently,  $\text{Cu}_3\text{P}$  formation takes place at very high P concentrations and this observation is in accordance with our previous work [44], where P contents were lower and  $\text{Cu}_3\text{P}$  formation was not observed.

Different annealing conditions also altered the crystallite size of the phosphide layers. The full-width-at-half-maximum (FWHM) of the (111) reflection (40.8°) was considered to calculate the mean crystallite size of the  $\text{Ni}_2\text{P}$  phase. The Scherrer equation yielded the values reported in Table 1. As expected, longer annealing times and higher temperatures led to larger crystallites.

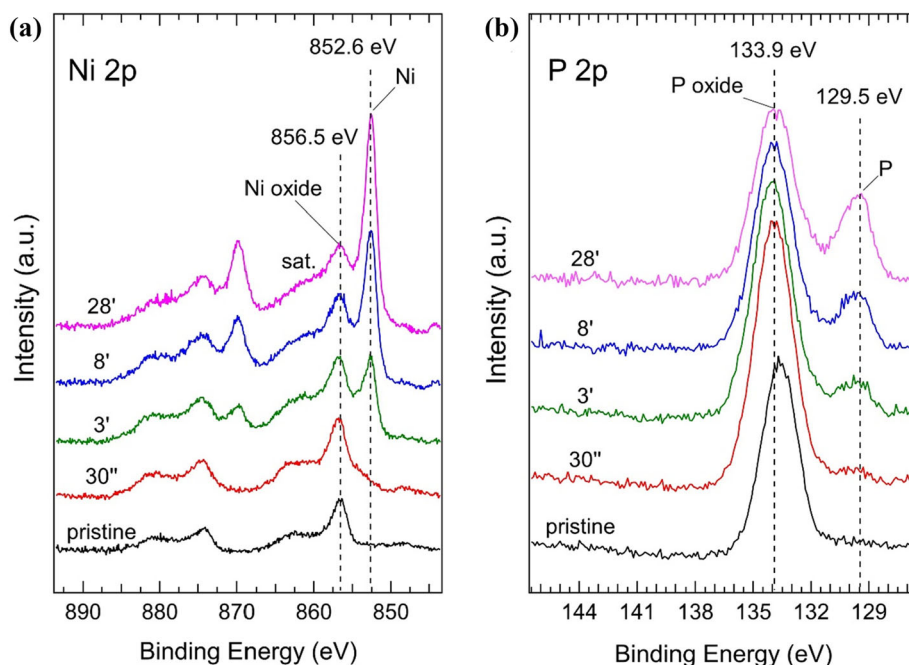
### XPS characterization

Diffraction analysis, even in glancing angle configuration, cannot provide detailed information about the

phase composition and the chemical state of the material present in the first few nm close to the surface. In order to determine the phases present in this region, XPS analysis was carried out on four samples, the first being a layer plated from the 100 g L<sup>-1</sup> solution and not annealed. This sample allowed to study the properties of the NiP/P codeposit before annealing. Then, three samples were characterized to investigate the influence of annealing time on the superficial properties of the electrocatalytic layers. These three samples were all plated from the 100 g L<sup>-1</sup> solution and subjected to three different annealing cycles: for 1 h at 300 °C, for 1 h at 400 °C and for 2 h at 300 °C. Data were acquired before and after sputtering, which was systematically carried out to remove the superficial oxide and to evaluate the properties of the material in the first few nm of thickness. Both high-resolution and survey spectra were acquired.

Figure 3 depicts the XPS characterization of the sample obtained from a 100 g L<sup>-1</sup> solution and not annealed. In analogy with our previous work [44], increasing sputtering times allowed to remove the oxide layer present on the surface of the sample. The cumulative sputtering time for each acquired spectrum is reported. The sputtering rate is evaluated to be around 3 nm/min, thus an overall layer of about 90 nm has been removed. Indeed, by looking at the Ni 2p spectra (Fig. 3a), it is evident that the peaks

**Figure 3** Waterfall plots of high-resolution XPS spectra at Ni 2p edge (a) and P 2p edge (b). Black spectra are from pristine samples. The cumulative sputtering for each acquisition is reported. The evaluated sputtering rate is 3 nm/min.



associated to the nickel in the form of solid solution [59] (metallic Ni  $2p_{3/2}$  peak at 852.6 eV and spin orbit splitting  $\Delta E = 17.1$  eV) progressively appeared and intensified as sputtering time increased. Conversely, the intensity of Ni  $2p_{3/2}$  peak at 856.5 eV, associated to nickel oxide, decreased. By looking at the spectra, a shake-up satellite for the pristine sample is placed at around 5.8 eV above the position of nickel oxide (856.6 eV) with a slight shift towards lower BE as the sputtering time increases. An analogous effect can be observed by considering the high-resolution P  $2p$  spectra (Fig. 3b), which were acquired concurrently with Ni  $2p$ . In this case, the intensity of the peak associated to P in solid solution (129.5 eV) progressively increased at the expenses of the peak of phosphorous oxide (133.9 eV). The positions of both Ni and P peaks are compatible with the values reported by Elsener et al. for Ni–P solid solutions [60]. The contribution of the red phosphorus dispersed inside the matrix cannot be clearly distinguished in the P  $2p$  peak due to its excessive overlapping with the contribution resulting from the solid solution. It is worth noticing that the oxidized P peak moves according to the sputtering time. This effect can be attributed to the presence, at variable depths, of P oxides characterized by different stoichiometries. Globally, the peak can be attributed to the 5 + oxidation state, but different contributions can come from species containing bonds of the P–O, P=O or P–O–P types [61, 62].

Following the non-annealed sample, the three layers subjected to different annealing cycles (1 h at 300 °C, 1 h at 400 °C, 2 h at 300 °C) were analysed (Fig. 4). The layers were sputtered for different times until a significant signal from the oxide-free components was recorded. The survey spectra for the three samples are presented in figure S8 and, by observing the peaks present, it is possible to get a clear indication of the effect of sputtering. Indeed, C 1s disappeared in all the samples after sputtering, indicating a total removal of carbonaceous contamination. In addition, the intensity of the O 1s peaks decreased after sputtering, indicating oxide removal from the surface. Regarding the high-resolution Ni  $2p$  spectra, the non-oxidized Ni feature was fitted with two peaks, one for  $\text{Ni}_{12}\text{P}_5$  and another for  $\text{Ni}_2\text{P}$  [44]. Coherently with the literature [60], a difference of 0.2 eV between the two peaks was imposed. This procedure made possible a quantitative estimation of the relative amount of the two phases ( $\text{Ni}_{12}\text{P}_5$  and

$\text{Ni}_2\text{P}$ ), allowing a direct comparison between samples annealed in different conditions. Indeed, also the remaining Ni  $2p$  features and their P  $2p$  counterparts were fitted. By exploiting the areas of the peaks, three relevant ratios were calculated: P–O/(P–O + P–Ni) (P as oxide vs. the sum of P as oxide and P chemically bonded to Ni),  $\text{Ni}_2\text{P}/\text{Ni}_{12}\text{P}_5$  and Ni–O/( $\text{Ni}_2\text{P} + \text{Ni}_{12}\text{P}_5$ ) (Ni as oxide vs. the sum of  $\text{Ni}_2\text{P}$  and  $\text{Ni}_{12}\text{P}_5$ ) are reported in Table 2.

Figure 4a, b show the XPS spectra recorded from the sample annealed at 400 °C for 1 h before and after 60 min of sputtering, respectively. Before sputtering, the sample was heavily oxidized. Ni  $2p$  related to the presence of non-oxidized metal could not be observed. At the end of the sputtering process, despite its 60 min duration, there was still a considerable percentage of oxide (ratio Ni–O/( $\text{Ni}_2\text{P} + \text{Ni}_{12}\text{P}_5$ ) = 0.99). This is a direct consequence of the high annealing temperature used and the high reactivity of P and Ni towards even minimal amounts of oxygen contamination. By looking at the fitting performed on the Ni  $2p$  peak, the effect of the annealing temperature on the relative weight of  $\text{Ni}_2\text{P}$  and  $\text{Ni}_{12}\text{P}_5$  can be seen. Indeed, the sputtered layer presents a substantial equimolarity between  $\text{Ni}_2\text{P}$  and  $\text{Ni}_{12}\text{P}_5$  (ratio  $\text{Ni}_2\text{P}/\text{Ni}_{12}\text{P}_5 = 1.06$ ). The situation is considerably different for the sample annealed at 300 °C for 1 h. In this case, 15 min of sputtering are enough to observe an almost oxide-free material (ratio Ni–O/( $\text{Ni}_2\text{P} + \text{Ni}_{12}\text{P}_5$ ) = 0.35). Furthermore, the phase analysis performed on the Ni  $2p$  peak evidenced a neat predominance of  $\text{Ni}_2\text{P}$  (ratio  $\text{Ni}_2\text{P}/\text{Ni}_{12}\text{P}_5 = 1.55$ ). Finally, the sample annealed at 300 °C for 2 h was analysed as a counterexample. The oxidation level is, in this case, intermediate between the two observed after the other annealing treatments (300 °C + 1 h and 400 °C + 1 h). After a sputtering time of 28 min 30 s, still some oxidized Ni was detectable on the surface (ratio Ni–O/( $\text{Ni}_2\text{P} + \text{Ni}_{12}\text{P}_5$ ) = 1.02). An intermediate situation can be observed also in the phase composition by fitting the Ni  $2p$  peak. In particular, it was possible to observe a predominance of  $\text{Ni}_2\text{P}$  in coexistence with a relevant percentage of  $\text{Ni}_{12}\text{P}_5$  (ratio  $\text{Ni}_2\text{P}/\text{Ni}_{12}\text{P}_5 = 1.15$ ).

Figure 5 depicts the results obtained by fitting the high-resolution P  $2p$  spectra. In analogy with what observed in the case of Ni, also P is present in its oxidized form at the surface. The two samples annealed at 400 °C for 1 h and 300 °C for 2 h present only oxidized P on the surface before sputtering

**Figure 4** High-resolution XPS spectra of Ni 2p.

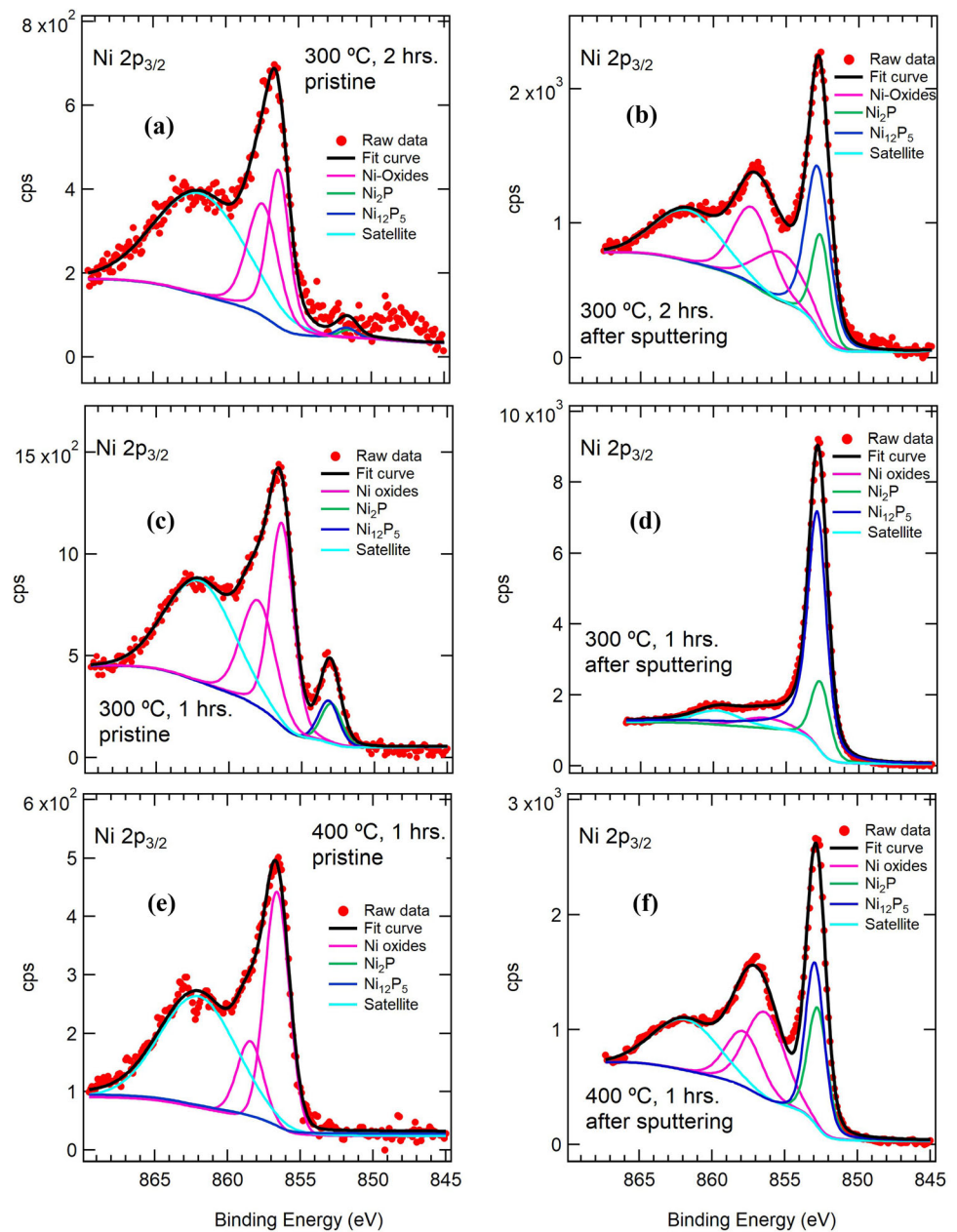


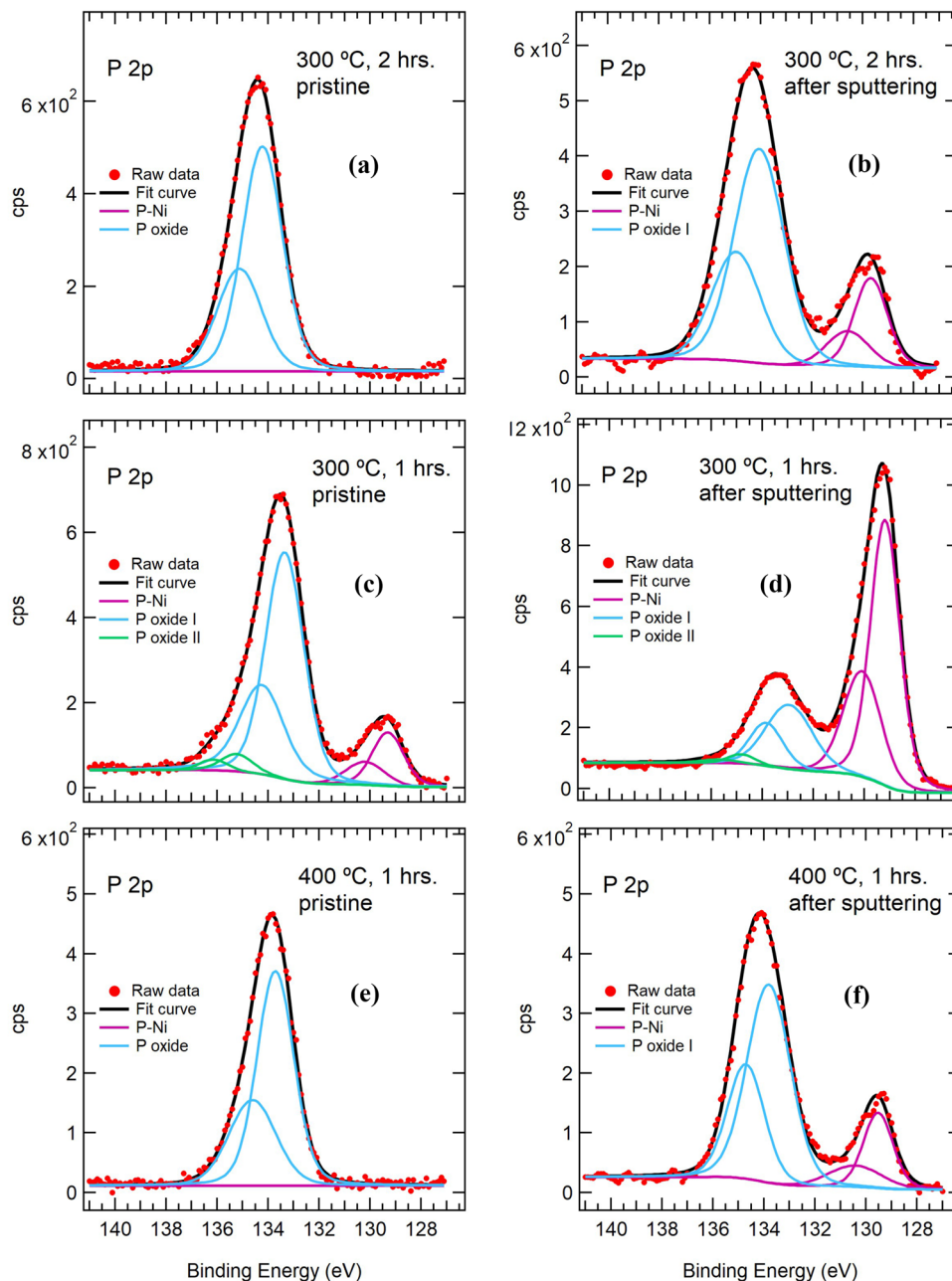
**Table 2** P–O/(P–O + P–Ni), Ni<sub>2</sub>P/Ni<sub>12</sub>P<sub>5</sub> and Ni–O/(Ni<sub>2</sub>P + Ni<sub>12</sub>P<sub>5</sub>) ratios calculated from the areas of the XPS fitted peaks

| Sample                              | Condition | P–O/(P–O + P–Ni) | Ni <sub>2</sub> P/Ni <sub>12</sub> P <sub>5</sub> | Ni–O/(Ni <sub>2</sub> P + Ni <sub>12</sub> P <sub>5</sub> ) |
|-------------------------------------|-----------|------------------|---|---|
| 100 g L <sup>-1</sup> ; 300 °C; 1 h | Pristine  | 0.84             | 1.00  | 1.25  |
| 100 g L <sup>-1</sup> ; 300 °C; 1 h | Sputtered | 0.29             | 1.55  | 0.35  |
| 100 g L <sup>-1</sup> ; 400 °C; 1 h | Pristine  | 1.00             | –   | –   |
| 100 g L <sup>-1</sup> ; 400 °C; 1 h | Sputtered | 0.79             | 1.06  | 0.99  |
| 100 g L <sup>-1</sup> ; 300 °C; 2 h | Pristine  | 1.00             | 1.00  | 1.28  |
| 100 g L <sup>-1</sup> ; 300 °C; 2 h | Sputtered | 0.78             | 1.15  | 1.02  |

(ratio P–O/(P–O + P–Ni) = 1). This is obvious also by looking at the corresponding XPS graphs (Fig. 5a, e), where only the peak around 133.9 eV can be seen.

The sample annealed at 300 °C for 1 h, conversely, presents a limited percentage of non-oxidized P on the surface (Fig. 5c; ratio P–O/(P–O + P–Ni) = 0.84).

**Figure 5** High resolution XPS spectra of P 2p.



After sputtering, the P-O/(P-O + P-Ni) ratio of all the sample decreased, revealing thus a higher amount of non-oxidized P in the deeper levels of the coating. XPS graphs (Fig. 5b, d, f) confirm this observation, with a visible increase of intensity for the P-Ni peaks around 129.5 eV. Regarding the sample annealed at 300 °C for 1 h, it is worth pointing out a peculiarity observed in the fitting of the P-O peak (Fig. 5c, d). It was not possible to correctly fit the peak by employing the same set of two peaks, corresponding to P 2p<sub>1/2</sub> and P 2p<sub>3/2</sub>, used for the other

samples. Indeed, a second set of P 2p<sub>1/2</sub> + P 2p<sub>3/2</sub> peaks was employed. The necessity to use these peaks, which corresponds to different oxidations states for P, reasonably stems from the presence of P oxides characterized by different stoichiometries. This effect, already argued from the shifting position of the P 2p peak in Fig. 3b, is connected to the presence of different XPS contributions coming from species containing bonds of the P-O, P=O or P-O-P types.



By comparing the information acquired from the bulk via XRD with those obtained from the external surface via XPS, it is possible to reconstruct the internal structure of the annealed NiP/P layers (figure S10). Moving from the Cu substrate towards the surface, XRD revealed the presence of an interfacial  $\text{Cu}_3\text{P}$  layer between Cu and NiP/P. Then, as demonstrated by XRD, the bulk of the layer consists of  $\text{Ni}_2\text{P}$ . The top portion (indicatively, the first few tens of nm below the surface) presents a concentration gradient for  $\text{Ni}_2\text{P}$ , whose relative quantity decreases moving towards the surface. In this region,  $\text{Ni}_2\text{P}$  coexists with  $\text{Ni}_{12}\text{P}_5$  in a proportion that depends on the annealing conditions. Finally, the external part of the sample results covered by a thin oxide layer, whose presence cannot be detected by XRD but only by XPS. Such layer is constituted by mixed oxides of P and Ni and its thickness is a function of the annealing temperature and duration.

### Electrocatalysis performances

The HER catalytic activity of the annealed NiP/P layers was assessed in a 0.5 M  $\text{H}_2\text{SO}_4$  solution. Tests were carried out following a standard methodology, which is described in literature for HER in acidic conditions. The effect of annealing time and temperature was investigated, together with the effect of codeposited P amount. The HER performance of the Cu substrate, of a 20 wt% Pt commercial catalyst and of a non-annealed NiP/P layer was evaluated for comparison.

Catalyst loading for the layers plated from the different electrolytes (20, 50 and 100  $\text{g L}^{-1}$ ) was determined as well. In general, the amount of the material deposited is proportional to the total charge, which is related to the current density (20  $\text{mA cm}^{-2}$ ) and the deposition time (2 h). However, the amount of codeposited P, which depends on the electrolyte used, determines the total amount of plated material. To calculate the catalyst loading, the amount of NiP/P plated from each bath was estimated as the weight difference (before and after plating) divided by the area of the deposit. The following values were obtained: 7.26  $\text{mg cm}^{-2}$  for the bath containing 20  $\text{g L}^{-1}$  of red P, 7.23  $\text{mg cm}^{-2}$  for the bath containing 50  $\text{g L}^{-1}$  of red P and 7.12  $\text{mg cm}^{-2}$  for the bath containing 100  $\text{g L}^{-1}$  of red P. As a general trend, lower values of catalyst loading were achieved

with the NiP/P layers containing the highest concentration of red P.

Figure 6a depicts the effect of two different annealing times (1 h and 2 h) at two distinct annealing temperatures (300 °C and 400 °C) on HER behaviour. In general, all the layers present relatively low values of the reference HER overpotential at 10  $\text{mA cm}^{-2}$  ( $\eta_{10}$ ), indicating varying degrees of electrocatalytic efficiency. Such values are reported in Table 3. Considering the four annealed samples analysed, the structure identified by XPS measurements can easily explain the behaviour observed. Indeed, the samples treated at 300 °C were characterized by a higher content of  $\text{Ni}_2\text{P}$  compared to the samples annealed at 400 °C and exhibited lower overpotentials. Between the two samples treated at 300 °C, the lower overpotential was recorded for the sample annealed for 1 h, which presents the higher  $\text{Ni}_2\text{P}$  percentage. Also the varying thickness of the oxide layer existing on the surface (figure S9) plays a fundamental role in electrocatalytic performances. The layer annealed at 300 °C for 1 h was characterized by the highest amount of  $\text{Ni}_2\text{P}$  at the surface and the thinnest layer of oxide. Consequently, it achieved the lowest overpotential (208.7 mV vs. RHE).

The effect of different annealing temperatures on HER overpotentials was investigated too (Fig. 6b). Keeping constant the annealing duration at 2 h and moving from 400 to 300 °C, a progressive decrease in the values of  $\eta_{10}$  was observed. Obviously, this effect is coherent with an increasing percentage of the more active phase ( $\text{Ni}_2\text{P}$ ) over the less active one ( $\text{Ni}_{12}\text{P}_5$ ). Interestingly, the curves related to annealing temperatures of 350 °C and 300 °C are almost superimposed, suggesting similar surface conditions.

Finally, the effect of the amount of codeposited P particles was studied (Fig. 6c). To this extent, three samples deposited from electrolytes loaded with increasing amounts of P particles were analysed: 20  $\text{g L}^{-1}$  (resulting in 43.6 at.% P in the layer before annealing), 50  $\text{g L}^{-1}$  (resulting in 52.2 at.% P in the layer before annealing) and 100  $\text{g L}^{-1}$  (resulting in 56 at.% P in the layer before annealing). As expected, strong variations in P content in the bath affected the amount of P codeposited in the layer and the electrocatalytic properties. With the bath load of 20  $\text{g L}^{-1}$ , the P content in the deposited layer was only 43.6 at.% and further decreased to 32.2 at.% after annealing. Consequently, P content was not enough to completely convert the layer material to

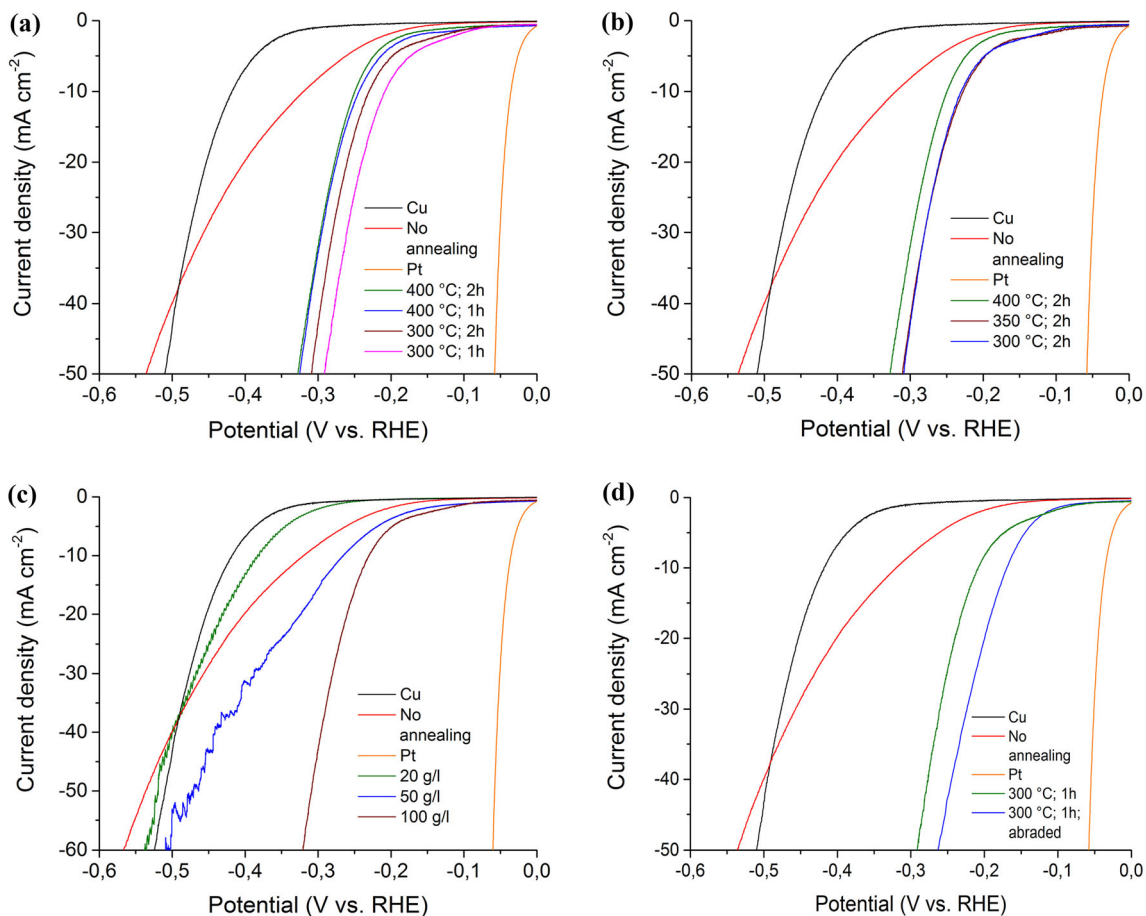


**Figure 6** HER behaviour of four NiP/P layers annealed at two different temperatures and durations (a); HER behaviour of three NiP/P layers annealed at three different temperatures (b); HER

behaviour of three NiP/P layers obtained from three different baths and annealed at 300 °C for 2 h (c); HER behaviour of a layer annealed a 300 °C for 1 h and mechanically abraded (d).

**Table 3** HER performance of the layers analysed

| P concentration in the bath (g L <sup>-1</sup> ) | Annealing temperature (°C) | Annealing time (h) | Concentration of P in the layer after annealing (at.%) | Overpotential $\eta_{10}$ (mV) | Notes        |
|--|----------------------------|--------------------|--|--------------------------------|--------------|
| –  | –                          | –                  | –  | 35.6                           | Pt reference |
| –  | –                          | –                  | –  | 418.2                          | Cu substrate |
| 100  | –                          | –                  | 56.0   | 320.2                          | Not annealed |
| 20   | 300                        | 2                  | 32.2   | 380.7                          | –            |
| 50   | 300                        | 2                  | 42.8   | 265.7                          | –            |
| 100  | 300                        | 1                  | 53.2   | 208.7                          | –            |
| 100  | 300                        | 2                  | 51.7   | 230.2                          | –            |
| 100  | 350                        | 2                  | 40.5   | 227.5                          | –            |
| 100  | 400                        | 2                  | 34.4   | 249.7                          | –            |
| 100  | 400                        | 1                  | 38.6   | 244.1                          | –            |
| 100  | 300                        | 1                  | –  | 169.5                          | Abraded      |

Ni<sub>2</sub>P. Furthermore, P concentration in the proximity of the surface was reasonably very low in this sample. Coherently with these observations, measured  $\eta_{10}$  was high. Overpotentials decreased as the bath load increased, and the catalyst prepared from the electrolyte with 100 g L<sup>-1</sup> P exhibited the lowest values.

By comparing the post-sputtering ratios shown in Table 2 for the three samples subjected to different annealing cycles (1 h at 300 °C, 1 h at 400 °C, 2 h at 300 °C) with the corresponding HER overpotentials reported in Table 3, a clear correlation can be identified. In general, low overpotentials are associated to high Ni<sub>2</sub>P/Ni<sub>12</sub>P<sub>5</sub> ratios and low Ni–O/(Ni<sub>2</sub>P + Ni<sub>12</sub>P<sub>5</sub>) ratios. For instance, the sample annealed at 300 °C for 1 h reached an overpotential equal to 208.7 mV vs. RHE in front of a Ni<sub>2</sub>P/Ni<sub>12</sub>P<sub>5</sub> ratio of 1.55 and a Ni–O/(Ni<sub>2</sub>P + Ni<sub>12</sub>P<sub>5</sub>) ratio of 0.35. On the other hand, the sample annealed at 400 °C for 1 h was characterized by an overpotential equal to 244.1 mV vs. RHE in front of a Ni<sub>2</sub>P/Ni<sub>12</sub>P<sub>5</sub> ratio of 1.06 and a Ni–O/(Ni<sub>2</sub>P + Ni<sub>12</sub>P<sub>5</sub>) ratio of 0.99. In the case of the sample annealed at 300 °C for 2 h, the situation is intermediate.

According to the results derived from the XPS analysis, it was expected to obtain better catalytic performance from the material immediately beneath the sample surface. Consequently, it was decided to evaluate HER performance of the layers by removing some of the material in the proximity of the surface. This can be done either chemically or mechanically. In the present work, a layer plated from the 100 g L<sup>-1</sup> P electrolyte was subjected to annealing for 1 h at 300 °C and then mechanically abraded with 1200 grit sand paper. Figure 6d visualizes the result obtained from the HER characterization of the abraded layer thus prepared. Compared to the as-annealed counterpart, the abraded coating achieved a significantly lower overpotential (169.5 mV vs. RHE). This happened because the superficial layer, which was Ni<sub>12</sub>P<sub>5</sub>-rich and oxide-rich, was removed by the polishing process (figure S9). Consequently, the measured  $\eta_{10}$  was in agreement with values reported in the literature for Ni<sub>2</sub>P [34, 63].

The overpotential–current curves displayed in Fig. 6 were replotted as Tafel plots to estimate the kinetic properties of the different materials. As shown in figure S11, the Tafel slope for the Ni<sub>2</sub>P containing layers (annealed at 300 °C for 1 h) varies according to the surface state. Tafel slope

significantly decrease moving from the non-abraded sample (108 mV dec<sup>-1</sup>) to the abraded one (80 mV dec<sup>-1</sup>). However, both values are lower than the slope exhibited by the non-annealed NiP/P sample (124 mV dec<sup>-1</sup>). These results suggest relatively favourable HER kinetics if compared to Pt performance (32 mV dec<sup>-1</sup>). Finally, the stability over time was evaluated. In particular, the layer deposited from the bath with 100 g L<sup>-1</sup> P, annealed at 300 °C for 1 h and then mechanically abraded was subjected to 200 cycles between 0 and –0.8 V vs. Ag/AgCl at 50 mV s<sup>-1</sup>. This catalyst exhibited a relatively good stability (figure S12); the overpotential difference between cycles 0 and 100 was 3.8 mV and became 10.6 mV between cycles 0 and 200.

### Comparison with other electrodeposited nickel phosphide thin layers

The results of the present work can be compared with the existing literature on HER in acidic media from thin electrodeposited layers based on transition metal phosphides [64]. Wasalathanthri et al. recently demonstrated the possibility to carry out HER on electrodeposited amorphous NiP films, which exhibited good performance in acidic media (0.5 M H<sub>2</sub>SO<sub>4</sub>) [65]. They were able to achieve a current density of 10 mA cm<sup>-2</sup> at the overpotential of 222 mV vs. RHE. Also Jiang et al. carried out similar tests, but in alkaline environment (1 M KOH). In this case, they were able to achieve overpotentials of 93 mV vs. RHE for HER [66]. The possibility to perform HER on ternary and quaternary Ni-based alloys has been demonstrated too. Chai et al., for example, deposited CoNiP for HER applications [67]. Their most active catalyst required an overpotential of 92 mV vs. RHE to reach a 10 mA cm<sup>-2</sup> current density; Wu et al. electrodeposited NiFeCMo [68] and exploited this alloy for HER, achieving an overpotential of 254 mV vs. RHE to drive a current density of 10 mA cm<sup>-2</sup>. It is in general difficult to establish a proper comparison between different electrocatalytic materials. Electrocatalytic efficiency depends on crystallite size in the case of thin layers, and on dimension and shape in the case of nanoparticles/nanowires. HER efficiency also depends on the electrochemically active surface area (ECSA) of the catalyst, which is typically not reported in most literature articles. Liu et al. [69] and Hu et al. [70], for example, prepared highly porous nickel phosphide

nanosheets under varying conditions and demonstrated a clear effect of their specific surface on final HER performances. In front of this evidence, the HER results obtained in the present work must be correlated to the relatively low ECSA of the layers, which are not nanostructured. Despite these difficulties, the record overpotential at  $10 \text{ mA cm}^{-2}$  current density observed in the present work (169.5 mV versus RHE) compares well with these literature results, suggesting a significant applicative potential for the technique here described.

## Conclusions

The present work advanced the knowledge on the production of nickel phosphide electrocatalytic layers via codeposition-annealing route. The NiP/P codeposition step was investigated and optimized, achieving a 56 at. % global concentration of P in the composite. After the codeposition step, NiP/P coatings were annealed to form electroactive compounds of Ni and P. Thanks to the support of two complementary techniques like XRD and XPS, the reaction kinetics and the phase modifications taking place in both the bulk and the surface of the layers were correctly identified. Whereas the bulk of the annealed coatings was composed of nearly pure  $\text{Ni}_2\text{P}$  phase, the surface was characterized by the coexistence of  $\text{Ni}_2\text{P}$  and  $\text{Ni}_{12}\text{P}_5$ . The ratio between these two phases was found to vary according to the annealing temperature and duration. Indeed, harsher annealing conditions were found to enhance P evaporation from the layer, leading thus to lower  $\text{Ni}_2\text{P}/\text{Ni}_{12}\text{P}_5$  ratios on the surface. XPS also evidenced the presence of oxidized Ni and P on the surface, whose predominance was favoured by annealing treatments performed at higher temperatures for longer times (as shown by the  $\text{NiO}/(\text{Ni}_2\text{P} + \text{Ni}_{12}\text{P}_5)$  ratio). All these features affected the electrocatalytic performances, with the samples characterized by the highest superficial  $\text{Ni}_2\text{P}/\text{Ni}_{12}\text{P}_5$  ratios and the lowest  $\text{NiO}/(\text{Ni}_2\text{P} + \text{Ni}_{12}\text{P}_5)$  ratios presenting the lowest HER overpotentials. In particular, a record overpotential of 208.7 mV versus RHE was observed at  $10 \text{ mA cm}^{-2}$  for the layers deposited from a  $100 \text{ g L}^{-1}$  red P electrolyte and annealed at  $300 \text{ }^\circ\text{C}$  for 1 h. Furthermore, it was demonstrated that even lower overpotentials could be reached by mechanically removing the outer layer, which was enriched in

$\text{Ni}_{12}\text{P}_5$  and oxides. In particular, a layer deposited from a  $100 \text{ g L}^{-1}$  red P electrolyte and annealed at  $300 \text{ }^\circ\text{C}$  for 1 h exhibited a 169.5 mV versus RHE overpotential at  $10 \text{ mA cm}^{-2}$  after mechanical abrasion. This sample was characterized by good HER kinetics, good stability over time and a general behaviour like that of pure  $\text{Ni}_2\text{P}$ . According to the results obtained, the nickel phosphide layers produced following the proposed methodology are attractive alternatives to Pt-based catalysts. However, the applicability of the codeposition-annealing technique here described is not strictly limited to nickel. In principle, the same approach can be applied to the production of CoP, FeP, CuP or MoP, which are all promising candidates as Pt-free electrocatalysts for water splitting.

## Data availability

Raw data are available from the authors upon reasonable request.

## Declarations

**Conflict of interest** All authors declare that they have no conflicts of interest.

**Open Access** This article is licensed under a Creative Commons Attribution 4.0 International License, which permits use, sharing, adaptation, distribution and reproduction in any medium or format, as long as you give appropriate credit to the original author(s) and the source, provide a link to the Creative Commons licence, and indicate if changes were made. The images or other third party material in this article are included in the article's Creative Commons licence, unless indicated otherwise in a credit line to the material. If material is not included in the article's Creative Commons licence and your intended use is not permitted by statutory regulation or exceeds the permitted use, you will need to obtain permission directly from the copyright holder. To view a copy of this licence, visit <http://creativecommons.org/licenses/by/4.0/>.

**Supplementary Information:** The online version contains supplementary material available at <https://doi.org/10.1007/s10853-022-07251-3>.



## References

- [1] Foley A, Olabi AG (2017) Renewable energy technology developments, trends and policy implications that can underpin the drive for global climate change. *Renew Sustain Energy Rev* 68:1112–1114
- [2] Amrouche SO, Rekioua D, Rekioua T, Bacha S (2016) Overview of energy storage in renewable energy systems. *Int J Hydrogen Energy* 41:20914–20927
- [3] Markovic NM (2013) Interfacing electrochemistry. *Nat Mater* 12:101–102
- [4] van Renssen S (2020) The hydrogen solution? *Nat Clim Change* 10:799–801
- [5] Brouwer J (2010) On the role of fuel cells and hydrogen in a more sustainable and renewable energy future. *Curr Appl Phys* 10:S9–S17
- [6] Züttel A, Remhof A, Borgschulte A, Friedrichs O (2010) Hydrogen: the future energy carrier. *Philos Trans R Soc A Math Phys Eng Sci* 368:3329–3342. <https://doi.org/10.1098/rsta.2010.0113>
- [7] Edwards PP, Kuznetsov VL, David WIF (2007) Hydrogen energy. *Philos Trans R Soc A Math Phys Eng Sci* 365:1043–1056
- [8] Kelly NA (2014) Hydrogen production by water electrolysis. In: Basile A and Iulianelli A (eds) *Advances in hydrogen production, storage and distribution*. Elsevier, Amsterdam, Netherland, pp 159–185
- [9] Ezaki H, Morinaga M, Watanabe S (1993) Hydrogen overpotential for transition metals and alloys, and its interpretation using an electronic model. *Electrochim Acta* 38:557–564. [https://doi.org/10.1016/0013-4686\(93\)85012-N](https://doi.org/10.1016/0013-4686(93)85012-N)
- [10] Eftekhari A (2017) Electrocatalysts for hydrogen evolution reaction. *Int J Hydrogen Energy* 42:11053–11077
- [11] Salonen LM, Petrovykh DY, Kolen'ko YV (2021) Sustainable catalysts for water electrolysis: Selected strategies for reduction and replacement of platinum-group metals. *Mater Today Sustain* 11:100060
- [12] Zheng Y, Jiao Y, Jaroniec M, Qiao SZ (2015) Advancing the electrochemistry of the hydrogen-evolution reaction through combining experiment and theory. *Angew Chem Int Ed* 54:52–65
- [13] Gong M, Wang DY, Chen CC et al (2016) A mini review on nickel-based electrocatalysts for alkaline hydrogen evolution reaction. *Nano Res* 9:28–46. <https://doi.org/10.1007/s12274-015-0965-x>
- [14] Brown DE, Mahmood MN, Man MCM, Turner AK (1984) Preparation and characterization of low overvoltage transition metal alloy electrocatalysts for hydrogen evolution in alkaline solutions. *Electrochim Acta* 29:1551–1556. [https://doi.org/10.1016/0013-4686\(84\)85008-2](https://doi.org/10.1016/0013-4686(84)85008-2)
- [15] Safizadeh F, Ghali E, Houlachi G (2015) Electrocatalysis developments for hydrogen evolution reaction in alkaline solutions—a review. *Int J Hydrogen Energy* 40:256–274. <https://doi.org/10.1016/j.ijhydene.2014.10.109>
- [16] Lv H, Xi Z, Chen Z et al (2015) A new core/shell NiAu/Au nanoparticle catalyst with Pt-like activity for hydrogen evolution reaction. *J Am Chem Soc* 137:5859–5862. <http://doi.org/10.1021/jacs.5b01100>
- [17] Li L, Zhang G, Wang B et al (2020) Electrochemical formation of PtRu bimetallic nanoparticles for highly efficient and pH-universal hydrogen evolution reaction. *J Mater Chem A* 8:2090–2098
- [18] Faber MS, Lukowski MA, Ding Q et al (2014) Earth-abundant metal pyrites (FeS<sub>2</sub>, CoS<sub>2</sub>, NiS<sub>2</sub>, and their alloys) for highly efficient hydrogen evolution and polysulfide reduction electrocatalysis. *J Phys Chem C* 118:21347–21356. <https://doi.org/10.1021/jp506288w>
- [19] Wang F, Li Y, Shifa TA et al (2016) Selenium-enriched nickel selenide nanosheets as a robust electrocatalyst for hydrogen generation. *Angew Chem Int Ed* 55:6919–6924. <https://doi.org/10.1002/anie.201602802>
- [20] Xiao P, Chen W, Wang X (2015) A review of phosphide-based materials for electrocatalytic hydrogen evolution. *Adv Energy Mater* 5:1–13. <https://doi.org/10.1002/aenm.201500985>
- [21] Du H, Kong RM, Guo X et al (2018) Recent progress in transition metal phosphides with enhanced electrocatalysis for hydrogen evolution. *Nanoscale* 10:21617–21624. <http://doi.org/10.1039/c8nr07891b>
- [22] Wang Y, Kong B, Zhao D et al (2017) Strategies for developing transition metal phosphides as heterogeneous electrocatalysts for water splitting. *Nano Today* 15:26–55. <https://doi.org/10.1016/j.nantod.2017.06.006>
- [23] Yu F, Zhou H, Huang Y et al (2018) High-performance bifunctional porous non-noble metal phosphide catalyst for overall water splitting. *Nat Commun* 9:1–9. <https://doi.org/10.1038/s41467-018-04746-z>
- [24] Ray A, Sultana S, Paramanik L, Parida KM (2020) Recent advances in phase, size, and morphology-oriented nanostructured nickel phosphide for overall water splitting. *J Mater Chem A* 8:19196–19245
- [25] Jin M, Zhang X, Shi R et al (2021) Hierarchical CoP@Ni<sub>2</sub>P catalysts for pH-universal hydrogen evolution at high current density. *Appl Catal B Environ* 296:120350
- [26] Chen W-F, Muckerman JT, Fujita E (2013) Recent developments in transition metal carbides and nitrides as hydrogen evolution electrocatalysts. *Chem Commun* 49:8896–8909
- [27] Owens-Baird B, Kolen'ko Y V., Kovnir K, (2018) Structure–activity relationships for Pt-free metal phosphide hydrogen

- evolution electrocatalysts. *Chem A Eur J* 24:7298–7311. <https://doi.org/10.1002/chem.201705322>
- [28] Huang Z, Chen Z, Chen Z et al (2014) Ni<sub>12</sub>P<sub>5</sub> nanoparticles as an efficient catalyst for hydrogen generation via electrolysis and photoelectrolysis. *ACS Nano* 8:8121–8129
- [29] Kucernak ARJ, Naranammalpuram Sundaram VN (2014) Nickel phosphide: the effect of phosphorus content on hydrogen evolution activity and corrosion resistance in acidic medium. *J Mater Chem A* 2:17435–17445. <https://doi.org/10.1039/c4ta03468f>
- [30] Wexler RB, Martinez JMP, Rappe AM (2017) Active role of phosphorus in the hydrogen evolving activity of nickel phosphide (0001) surfaces. *ACS Catal* 7:7718–7725
- [31] Park J, Koo B, Yoon KY et al (2005) Generalized synthesis of metal phosphide nanorods via thermal decomposition of continuously delivered metal–phosphine complexes using a syringe pump. *J Am Chem Soc* 127:8433–8440. <https://doi.org/10.1021/ja0427496>
- [32] Read CG, Callejas JF, Holder CF, Schaak RE (2016) General strategy for the synthesis of transition metal phosphide films for electrocatalytic hydrogen and oxygen evolution. *ACS Appl Mater Interfaces* 8:12798–12803
- [33] Liu P, Zhang Z-X, Jun SW et al (2019) Controlled synthesis of nickel phosphide nanoparticles with pure-phase Ni<sub>2</sub>P and Ni<sub>12</sub>P<sub>5</sub> for hydrogenation of nitrobenzene. *React Kinet Mech Catal* 126:453–461
- [34] Wang X, Kolen'ko YV, Liu L (2015) Direct solvothermal phosphorization of nickel foam to fabricate integrated Ni<sub>2</sub>P-nanorods/Ni electrodes for efficient electrocatalytic hydrogen evolution. *Chem Commun* 51:6738–6741. <https://doi.org/10.1039/c5cc00370a>
- [35] Liu Z, Huang X, Zhu Z, Dai J (2010) A simple mild hydrothermal route for the synthesis of nickel phosphide powders. *Ceram Int* 36:1155–1158. <https://doi.org/10.1016/j.ceramint.2009.12.015>
- [36] Zhang G, Xu Q, Liu Y et al (2020) Red phosphorus as self-template to hierarchical nanoporous nickel phosphides toward enhanced electrocatalytic activity for oxygen evolution reaction. *Electrochim Acta*. <https://doi.org/10.1016/j.electacta.2019.135500>
- [37] Xiao J, Lv Q, Zhang Y et al (2016) One-step synthesis of nickel phosphide nanowire array supported on nickel foam with enhanced electrocatalytic water splitting performance. *RSC Adv* 6:107859–107864
- [38] Wang X, Kolen'ko Y V, Bao X, et al (2015) One-step synthesis of self-supported nickel phosphide nanosheet array cathodes for efficient electrocatalytic hydrogen generation. *Angew Chemie Int Ed* 54:8188–8192
- [39] Wang X, Li W, Xiong D et al (2016) Bifunctional nickel phosphide nanocatalysts supported on carbon fiber paper for highly efficient and stable overall water splitting. *Adv Funct Mater* 26:4067–4077
- [40] Wang X, Li W, Xiong D, Liu L (2016) Fast fabrication of self-supported porous nickel phosphide foam for efficient, durable oxygen evolution and overall water splitting. *J Mater Chem A* 4:5639–5646
- [41] Xing J, Zou Z, Guo K, Xu C (2018) The effect of phosphating time on the electrocatalytic activity of nickel phosphide nanorod arrays grown on Ni foam. *J Mater Res* 33:556–567
- [42] Bains W, Petkowski JJ, Sousa-Silva C, Seager S (2019) Trivalent phosphorus and phosphines as components of biochemistry in anoxic environments. *Astrobiology* 19:885–902
- [43] Sparling DW, Day D, Klein P (1999) Acute toxicity and sublethal effects of white phosphorus in mute swans, *Cygnus olor*. *Arch Environ Contam Toxicol* 36:316–322
- [44] Bernasconi R, Khalil MI, Jaquinta C et al (2020) Nickel phosphides fabricated through a codeposition-annealing technique as low-cost electrocatalytic layers for efficient hydrogen evolution reaction. *ACS Appl Energy Mater* 3:6525–6535
- [45] Lelevic A, Walsh FC (2019) Electrodeposition of Ni-P alloy coatings: a review. *Surf Coatings Technol* 369:198–220. <https://doi.org/10.1016/j.surfcoat.2019.03.055>
- [46] Alleg S, Boussaha A, Tebib W et al (2016) Microstructure and magnetic properties of NiP alloys. *J Supercond Nov Magn* 29:1001–1011
- [47] Baer DR, Engelhard MH (2010) XPS analysis of nanostructured materials and biological surfaces. *J Electron Spectros Relat Phenomena* 178:415–432
- [48] Okamoto Y, Nitta Y, Imanaka T, Teranishi S (1979) Surface characterisation of nickel boride and nickel phosphide catalysts by X-ray photoelectron spectroscopy. *J Chem Soc Faraday Trans 1 Phys Chem Condens Phases* 75:2027–2039
- [49] Tiwari AP, Lee K, Kim K et al (2020) Conformally coated nickel phosphide on 3D, ordered nanoporous nickel for highly active and durable hydrogen evolution. *ACS Sustain Chem Eng* 8:17116–17123
- [50] Sun T, Dong J, Huang Y et al (2018) Highly active and stable electrocatalyst of Ni<sub>2</sub>P nanoparticles supported on 3D ordered macro-/mesoporous Co-N-doped carbon for acidic hydrogen evolution reaction. *J Mater Chem A* 6:12751–12758. <https://doi.org/10.1039/c8ta03672a>
- [51] Xin H, Guo K, Li D et al (2016) Production of high-grade diesel from palmitic acid over activated carbon-supported nickel phosphide catalysts. *Appl Catal B Environ* 187:375–385

- [52] Hovestad A, Janssen LJJ (1995) Electrochemical codeposition of inert particles in a metallic matrix. *J Appl Electrochem* 25:519–527
- [53] Łosiewicz B (2015) Electrodeposition mechanism of composite coatings. *Solid State Phenom* 228:65–78. <https://doi.org/10.4028/www.scientific.net/SSP.228.65>
- [54] Guglielmi N (1971) Kinetics of the deposition of inert particles from electrolytic baths. *J Electrochem Soc* 1501:1009–1012
- [55] Berçot P, Pea-Muoz E, Pagetti J (2002) Electrolytic composite Ni-PTFE coatings: an adaptation of Guglielmi's model for the phenomena of incorporation. *Surf Coat Technol* 157:282–289. [https://doi.org/10.1016/S0257-8972\(02\)00180-9](https://doi.org/10.1016/S0257-8972(02)00180-9)
- [56] Shrestha NK, Takebe T, Saji T (2006) Effect of particle size on the co-deposition of diamond with nickel in presence of a redox-active surfactant and mechanical property of the coatings. *Diam Relat Mater* 15:1570–1575. <https://doi.org/10.1016/j.diamond.2005.12.040>
- [57] Bernasconi R, Allievi F, Sadeghi H, Magagnin L (2017) Codeposition of nickel–phosphorus alloys reinforced with boron carbide microparticles: direct and pulse plating. *Trans IMF* 95:52–59
- [58] Okamoto H (2010) Ni–P (nickel–phosphorus). *J Phase Equilibria Diffus* 31:200–201
- [59] Biesinger MC, Payne BP, Lau LWM et al (2009) X-ray photoelectron spectroscopic chemical state quantification of mixed nickel metal, oxide and hydroxide systems. *Surf Interface Anal Int J Dev Appl Tech Anal Surf Interfaces Thin Film* 41:324–332
- [60] Elsener B, Atzei D, Krolkowski A, Rossi A (2008) Effect of phosphorus concentration on the electronic structure of nanocrystalline electrodeposited Ni–P alloys: an XPS and XAES investigation. *Surf Interface Anal* 40:919–926. <https://doi.org/10.1002/sia.2802>
- [61] Shimizu M, Tsushima Y, Arai S (2017) Electrochemical Na-insertion/extraction property of Ni-coated black phosphorus prepared by an electroless deposition method. *ACS Omega* 2:4306–4315
- [62] Sherwood PMA (2002) Introduction to studies of phosphorus-oxygen compounds by XPS. *Surf Sci Spectra* 9:62–66
- [63] Pan Y, Liu Y, Zhao J et al (2015) Monodispersed nickel phosphide nanocrystals with different phases: synthesis, characterization and electrocatalytic properties for hydrogen evolution. *J Mater Chem A* 3:1656–1665
- [64] Hu C, Lv C, Liu S et al (2020) Nickel phosphide electrocatalysts for hydrogen evolution reaction. *Catalysts*. <https://doi.org/10.3390/catal10020188>
- [65] Wasalathanthri RN, Jeffrey S, Su N et al (2017) Stoichiometric control of electrocatalytic amorphous nickel phosphide to increase hydrogen evolution reaction activity and stability in acidic medium. *ChemistrySelect* 2:8020–8027
- [66] Jiang N, You B, Sheng M, Sun Y (2016) Bifunctionality and mechanism of electrodeposited nickel–phosphorous films for efficient overall water splitting. *ChemCatChem* 8:106–112
- [67] Chai L, Liu S, Pei S, Wang C (2021) Electrodeposited amorphous cobalt-nickel-phosphide-derived films as catalysts for electrochemical overall water splitting. *Chem Eng J* 420:129686. <https://doi.org/10.1016/j.cej.2021.129686>
- [68] Wu Y, He H (2019) Electrodeposited nickel–iron–carbon–molybdenum film as efficient bifunctional electrocatalyst for overall water splitting in alkaline solution. *Int J Hydrogen Energy* 44:1336–1344. <https://doi.org/10.1016/j.ijhydene.2018.11.168>
- [69] Liu S, Hu C, Lv C et al (2019) Facile preparation of large-area self-supported porous nickel phosphide nanosheets for efficient electrocatalytic hydrogen evolution. *Int J Hydrogen Energy* 44:17974–17984. <https://doi.org/10.1016/j.ijhydene.2019.05.100>
- [70] Hu C, Cai J, Liu S et al (2020) General strategy for preparation of porous nickel phosphide nanosheets on arbitrary substrates toward efficient hydrogen generation. *ACS Appl Energy Mater* 3:1036–1045. <https://doi.org/10.1021/acsami.9b02067>

**Publisher's Note** Springer Nature remains neutral with regard to jurisdictional claims in published maps and institutional affiliations.